

This document is confidential and is proprietary to the American Chemical Society and its authors. Do not copy or disclose without written permission. If you have received this item in error, notify the sender and delete all copies.

Bottom-Up Synthesis of Liquid-Phase-Processable Graphene Nanoribbons with Near-Infrared Absorption

Journal:	ACS Nano
Manuscript ID:	nn-2014-049014.R2
Manuscript Type:	Article
Date Submitted by the Author:	21-Oct-2014
Complete List of Authors:	Narita, Akimitsu; Max-Planck-Institute for Polymer Research, Verzhbitskiy, Ivan; Free University Berlin, Department of Physics Frederickx, Wout; Katholieke Universiteit Leuven, Department of Chemistry Mali, Kunal; Katholieke Universiteit Leuven, Department of Chemistry Jensen, Soeren; Max Planck Institute for Polymer Research, Molecular Spectroscopy Hansen, Michael Ryan; Max-Planck-Institute for Polymer Research, Bonn, Mischa; Max Planck Institute for Polymer Research, Molecular spectroscopy De Feyter, Steven; KU Leuven, Department of Chemistry Casiraghi, Cinzia; University of Manchester, School of Chemistry Feng, Xinliang; Dresden University of Technology, Molecular Functional Materials Müllen, Klaus; Max-Planck-Institute for Polymer Research,

SCHOLARONE™
Manuscripts

Bottom-Up Synthesis of Liquid-Phase-Processable Graphene Nanoribbons with Near-Infrared Absorption

*Akimitsu Narita,[†] Ivan A. Verzhbitskiy,[‡] Wout Frederickx,[§] Kunal S. Mali,[§] Soeren Alkaersig
Jensen,^{†,||} Michael Ryan Hansen,^{†,⊥} Mischa Bonn,[†] Steven De Feyter,[§] Cinzia Casiraghi,^{‡,¶}
Xinliang Feng,^{*†} and Klaus Müllen^{*†}*

[†]Max Planck Institute for Polymer Research, Ackermannweg 10, D-55128 Mainz, Germany

[‡]Department of Physics, Free University Berlin, Arnimalle 14, 14195 Berlin, Germany

[§]Division of Molecular Imaging and Photonics, Department of Chemistry, KU Leuven-
University of Leuven, Celestijnenlaan, 200 F, B-3001 Leuven, Belgium

^{||}FOM Institute AMOLF, Science Park 104, 1098 XG Amsterdam, The Netherlands

[⊥]Interdisciplinary Nanoscience Center (iNANO) and Department of Chemistry, Aarhus
University, Gustav Wieds Vej 14, DK-8000 Aarhus C, Denmark

[¶]School of Chemistry, Manchester University, Oxford Road, Manchester, M139PL, United
Kingdom

*Address correspondence to muellen@mpip-mainz.mpg.de; feng@mpip-mainz.mpg.de.

1
2
3 KEYWORDS: graphene nanoribbon · cyclodehydrogenation · Diels–Alder reaction · bandgap
4
5 engineering · near-infrared absorption
6
7
8
9

10
11 ABSTRACT. Structurally defined, long (>100 nm), and low-bandgap (~1.2 eV) graphene
12
13 nanoribbons (GNRs) were synthesized through a bottom-up approach, enabling GNRs with a
14
15 broad absorption spanning into the near-infrared (NIR) region. The chemical identity of GNRs
16
17 was validated by IR, Raman, solid-state NMR, and UV–vis–NIR absorption spectroscopy.
18
19 Atomic force microscopy revealed well-ordered self-assembled monolayers of uniform GNRs on
20
21 a graphite surface upon deposition from the liquid phase. The broad absorption of the low-
22
23 bandgap GNRs enables their detailed characterization by Raman and time-resolved terahertz
24
25 photoconductivity spectroscopy with excitation at multiple wavelengths, including the NIR
26
27 region, which provides further insights into the fundamental physical properties of such graphene
28
29 nanostructures.
30
31
32
33
34
35
36
37
38
39

40 Graphene nanoribbons (GNRs), nano-strips of graphene, are emerging materials of great
41
42 promise, which possess non-zero bandgaps in stark contrast to semi-metallic graphene.^{1, 2} The
43
44 electronic properties such as the bandgaps of the GNRs critically depend on their width and edge
45
46 structures,³⁻⁶ which makes it crucial to precisely control the GNR structures for fundamental
47
48 studies as well as for future nanoelectronic applications. GNRs are typically prepared through
49
50 “top-down” approaches such as lithographic patterning of graphene sheets⁷⁻⁹ and unzipping of
51
52 carbon nanotubes,¹⁰⁻¹² revealing promising electronic properties of the GNRs. However, these
53
54 methods cannot avoid high structural disorder, especially at the edges of the resulting GNRs, and
55
56
57
58
59
60

often lack uniformity in the width. On the other hand, “bottom-up” chemical synthesis can provide a variety of structurally well-defined GNRs based on solution-mediated¹³⁻¹⁹ or surface-assisted²⁰⁻²³ cyclodehydrogenation of tailor-made polyphenylene precursors.

Whereas the GNRs previously prepared through the bottom-up methods were limited by the short length (<50 nm)¹³⁻¹⁵ and/or the necessity of metal surfaces,²⁰⁻²² we have very recently reported a solution synthesis of structurally well-defined GNR **1** with high longitudinal extension over 200 nm (Figure 1).¹⁶ We have employed an efficient *AB*-type Diels–Alder polymerization for the preparation of corresponding polyphenylene precursors with exceptionally large molecular weights, followed by intramolecular oxidative cyclodehydrogenation. Notably, GNR **1** shows a defined bandgap, in stark contrast to carbon nanotubes (CNTs) that are unavoidably obtained as a mixture of different diameters and chiralities with a corresponding wide distribution of bandgaps.^{24, 25} Nevertheless, the width of GNR **1** is limited to ~1 nm, corresponding to a bandgap of ~1.9 eV, with an optical absorption only up to ~650 nm.¹⁶

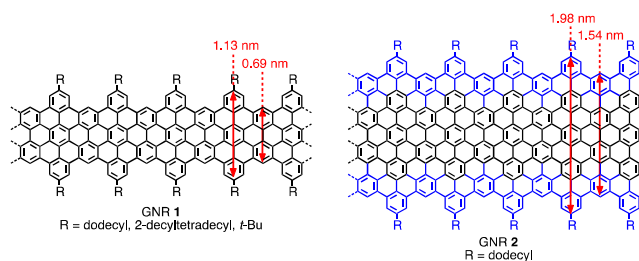


Figure 1. Structures of GNRs **1** and **2**. Geometric dimensions were derived from Merck Molecular Force Field 94 (MMFF94) calculations.

For the future development of GNR-based electronics and opto-electronics, it is highly important to tune the GNR width and thus the bandgaps, while maintaining the large longitudinal extension.^{5, 26} Specifically, a smaller bandgap leads to absorption over a wider range of

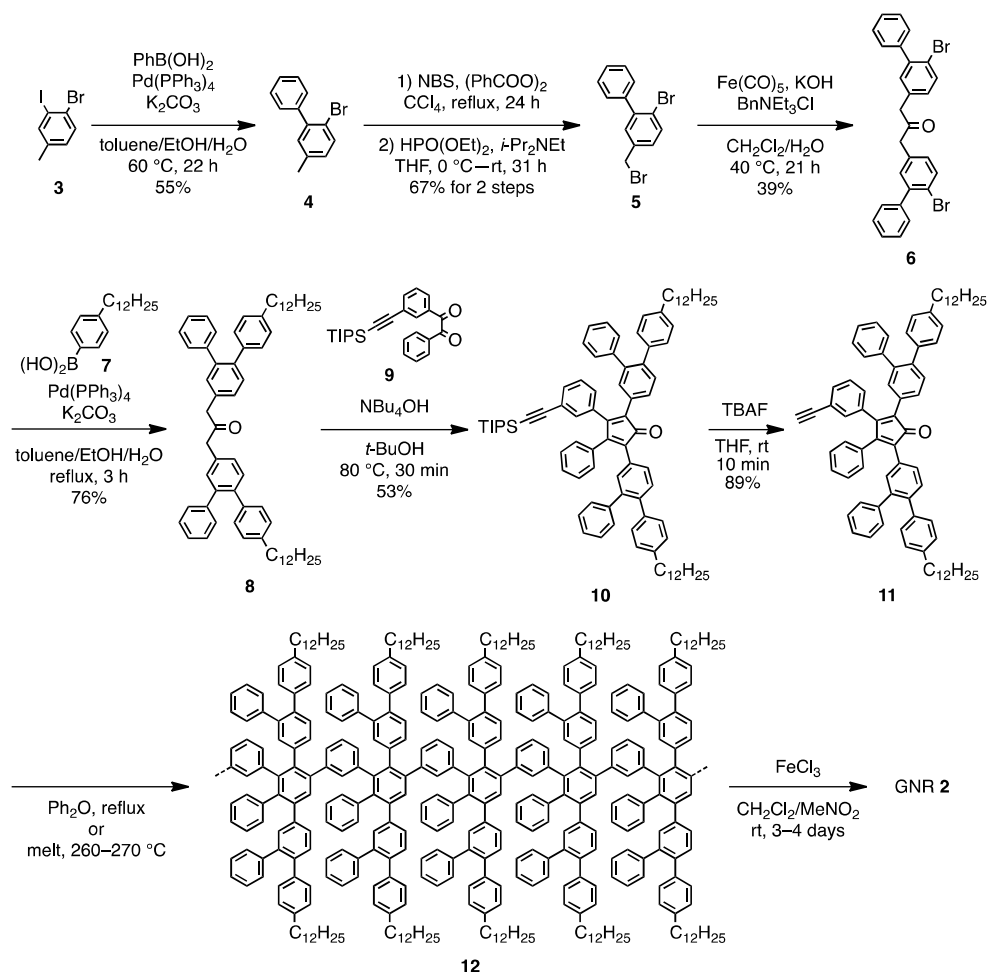
1
2
3 wavelengths, possibly including the near-infrared (NIR) region, which opens up possibilities for
4 various applications, including photovoltaics.^{5, 27} Moreover, GNRs with NIR absorption are
5 desirable to spectroscopically obtain an in-depth understanding on the basic physical properties
6 of the GNRs. For instance, Raman measurements at multiple wavelengths provide information
7 on the phononic and electronic dispersions of the GNRs, based on the resonant nature of the
8 Raman scattering process in GNRs.²⁸ In this article, we describe the synthesis and
9 characterization of GNR **2** with an extended width of ~2 nm and lengths exceeding 100 nm
10 (Figure 1). GNR **2** demonstrates a low and well-defined bandgap of ~1.2 eV with broad optical
11 absorption, extending into the NIR region, in contrast to the relatively large bandgap of GNR **1**.
12 Such GNRs with NIR absorption allow for in-depth investigations using multi-wavelength
13 Raman spectroscopy and ultrafast terahertz (THz) photoconductivity measurements.
14
15
16
17
18
19
20
21
22
23
24
25
26
27
28
29
30
31

32 RESULTS AND DISCUSSION

33
34
35 **Bottom-up solution synthesis of GNR 2.** In order to synthesize GNR **2** through an efficient
36 *AB*-type Diels–Alder polymerization, a laterally extended monomer **11** was designed, with a
37 cyclopentadienone moiety and an ethynyl group as the conjugated diene and the dienophile,
38 respectively (Scheme 1). 2-Bromo-5-methylbiphenyl (**4**) was prepared by selective Suzuki
39 coupling of 4-bromo-3-iodotoluene (**3**) with phenylboronic acid at 60 °C, and then brominated
40 with an excess amount of *N*-bromosuccinimide (NBS) to give a mixture of 2-bromo-5-
41 bromomethylbiphenyl (**5**) and 2-bromo-5-dibromomethylbiphenyl. The crude mixture was
42 subsequently treated with HPO(OEt)₂ and *i*-Pr₂NEt for selective debromination at the benzylic
43 position²⁹ to afford **5** in 67 % yield for two steps. Phase-transfer carbonylation of **5** with Fe(CO)₅
44 provided bis(bromobiphenyl)acetone **6** in 39 % yield, which was reacted with dodecylphenyl
45
46
47
48
49
50
51
52
53
54
55
56
57
58
59
60

boronic acid (**7**) via Suzuki coupling to obtain bis(*o*-terphenyl)acetone **8** in 76 % yield. Finally, Knoevenagel condensation of **8** with benzil **9**¹⁷ and subsequent removal of the triisopropylsilyl protecting group afforded the laterally extended monomer **11** in 47 % yield for two steps.

Scheme 1. Synthetic route toward GNR **2**.



AB-type Diels–Alder polymerization of monomer **11** was performed either by refluxing in diphenyl ether or heating at 260–270 °C in a melt to provide polyphenylene precursor **12**. Precursor **12** contained small oligomers upon preparation, according to size exclusion

1
2
3 chromatography (SEC) analysis, but such oligomers could be removed by fractionation with
4 recycling preparative SEC (see Supporting Information for details). When monomer **11** was
5 refluxed in diphenyl ether at a concentration of 221 mM, precursor **12-I** with weight-average
6 molecular weight (M_w) of 42000–78000 g·mol⁻¹ and polydispersity index (PDI) of 1.4–1.5 was
7 obtained after the removal of the smaller oligomers, based on SEC analysis against poly(*para*-
8 phenylene) (PPP) and polystyrene (PS) standards (Table S1, entry 1'). Although the M_w values
9 obtained by SEC analysis are only estimations based on the PPP and PS standard calibrations,
10 they are useful for effectively comparing the molecular weights of different polyphenylene
11 precursors.¹⁶

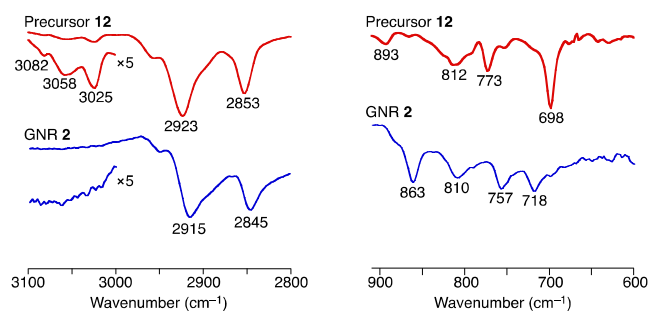
12
13
14
15
16
17
18
19
20
21
22
23
24
25
26
27
28
29
30
31
32
33
34
35
36
37
38
39
40
41
42
43
44
45
46
47
48
49
50
51
52
53
54
55
56
57
58
59
60

Notably, the polymerization of monomer **11** in a melt led to precursor **12-II** with a significantly higher M_w of 230000–550000 g·mol⁻¹ with PDI of 2.8–3.8 after removing the smaller oligomers by the preparative SEC (Table S1, entry 3'). This result is consistent with previous reports that polymers with larger molecular weight can be obtained when the Diels–Alder polymerization is carried out at higher monomer concentrations or in a melt.^{16, 30, 31} This M_w is comparable to the largest value obtained for the precursor of GNR **1**,¹⁶ and demonstrates the extremely high efficiency of *AB*-type Diels–Alder polymerization, also for the laterally extended system.

Subsequently, polyphenylene precursors **12-I** and **12-II** were “graphitized” into GNRs **2-I** and **2-II**, respectively, through oxidative cyclodehydrogenation with iron (III) chloride (Scheme 1). Precursor **12** contained numerous regioisomers, considering the two possible molecular orientations of unsymmetrical monomer **11** upon each cycloaddition step (Figure S4). Nevertheless, all the isomers lead to the identical GNR structure upon planarization (Figure S4). Based on the M_w of precursors **12-I** and **12-II**, the average lengths of GNRs **2-I** and **2-II** could

1
2
3 be estimated to be ca. 30–56 and 160–390 nm, respectively. Although these values are only
4
5
6 estimations, they indicated that GNR **2-II** is at least around three times longer than GNR **2-I**.
7
8
9

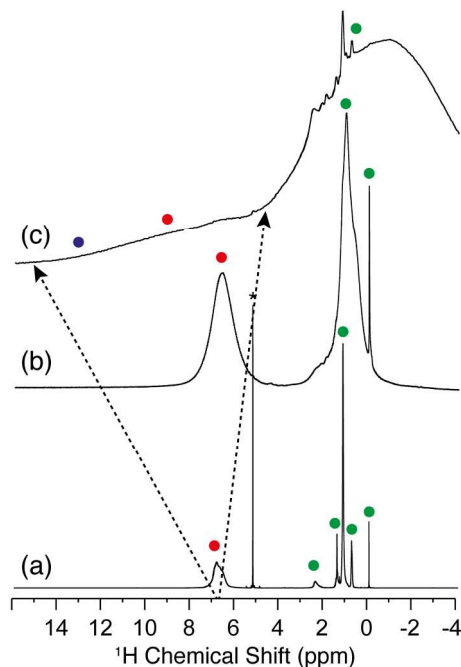
10 **FTIR and NMR spectroscopic characterization of precursor 12 and GNR 2.** The
11 efficiency of the cyclodehydrogenation was first examined by Fourier transform infrared (FTIR)
12 spectroscopic analysis (Figures 2 and S5). A comparison of the FTIR spectra of precursor **12** and
13 GNR **2** revealed the strong attenuation of the signal triad from aromatic C-H stretching
14 vibrations at 3025, 3058, and 3082 cm^{-1} , as well as the disappearance of out-of-plane (*opla*) C-H
15 deformation bands at 698, 773, and 893 cm^{-1} , which are characteristic for mono- and di-
16 substituted benzene rings (Figure 2).^{15, 16} Moreover, the band appearing at 863 cm^{-1} could be
17 assigned to the *opla* band from the aromatic C-H moiety at the cove position (see Figure 4d),
18 supporting the successful conversion of precursor **12** into GNR **2**.^{16, 32}
19
20
21
22
23
24
25
26
27
28
29
30
31
32
33



45 **Figure 2.** Representative FTIR spectral regions of polyphenylene precursor **12** (red) and GNR **2**
46 (blue).
47
48
49

50 Solid-state ^1H and ^{13}C magic-angle spinning (MAS) NMR spectroscopy^{33, 34} was employed to
51 further characterize precursor **12** and GNR **2** (Figures 3 and 4). The overall ^1H line width from
52 the aromatic protons of precursor **12**, centered at ~ 6.8 ppm, was similar in solution and in the
53
54
55
56
57
58
59
60

1
2
3 solid state, which indicated its relatively flexible structure (Figure 3a and b). In contrast, the ^1H
4 MAS NMR spectrum of GNR **2** showed significantly broadened and shifted aromatic and
5
6 MAS NMR spectrum of GNR **2** showed significantly broadened and shifted aromatic and
7
8 aliphatic ^1H resonances, corroborating the rigid and planar feature of GNR **2** with extended π -
9
10 conjugation (Figure 3c).³⁵⁻³⁷
11



37
38 **Figure 3** Liquid- and solid-state ^1H NMR spectra of (a) precursor **12** dissolved in CD_2Cl_2 , and
39
40 (b), (c) solid samples of precursor **12** and GNR **2**, respectively. The liquid-state NMR spectrum
41
42 in (a) was acquired at 7.05 T (300.13 MHz for ^1H), while the solid-state NMR experiments in (b)
43
44 and (c) were recorded at 20.0 T (850.26 MHz for ^1H) using a MAS frequency of 59524 Hz. The
45
46 asterisks in (a) mark the residual proton signal of CD_2Cl_2 . The dashed arrows illustrate the large
47
48 spread of ^1H chemical shifts in GNR **2** compared to **12** in solution.
49
50
51

52
53
54 2D ^1H - ^1H double quantum-single quantum (DQ-SQ) MAS NMR correlation experiments were
55
56 also performed to probe the spatial proximity between different protons *via* dipole-dipole
57
58
59
60

1
2
3 interactions (Figure 4a and b).^{38, 39} In agreement with the relatively flexible structure, the 2D ¹H-
4 ¹H DQ-SQ MAS NMR spectrum of precursor **12** only showed narrow ¹H-¹H correlation signals
5
6 between the aromatic protons as well as between the aromatic and aliphatic protons (Figure 4a).
7
8 On the other hand, GNR **2** displayed a broad, stretched, and split ridge of ¹H-¹H correlation
9
10 signals close to the spectrum diagonal (SQ_{iso}~7–15 ppm), in addition to a broad range of ¹H-¹H
11
12 correlation signals between aromatic and aliphatic protons (SQ_{iso}~4–12 ppm) (Figure 4b). On the
13
14 basis of the correlations to the aliphatic protons, the lower- and higher-frequency parts of the
15
16 aromatic signals could be assigned to the outer (red circle) and the inner (blue circle) proton,
17
18 respectively (Figure 4b and d). Interestingly, the spectral features observed for GNR **2** are
19
20 broader than those of narrower GNR **1**,¹⁶ most likely due to larger aromatic currents induced by
21
22 the extended aromatic cores.
23
24
25
26
27
28

29 Additionally, a 1D ¹³C{¹H} REcoupled Polarization-Transfer Heteronuclear Single
30
31 Quantum Correlation (REPT-HSQC) spectrum of GNR **2** was measured (Figure 4c).⁴⁰ By using
32
33 a short recoupling time, only ¹³C signals from the carbons situated at and near the edges were
34
35 observed. The spectrum showed three relatively broad ¹³C signals, which could be assigned to
36
37 aliphatic side chains (~30 ppm) as well as aromatic CH (~124 ppm) and quaternary aromatic
38
39 carbons (~139 ppm) at or close to the edges, based on their chemical shifts and intensities.
40
41
42
43
44
45
46
47
48
49
50
51
52
53
54
55
56
57
58
59
60

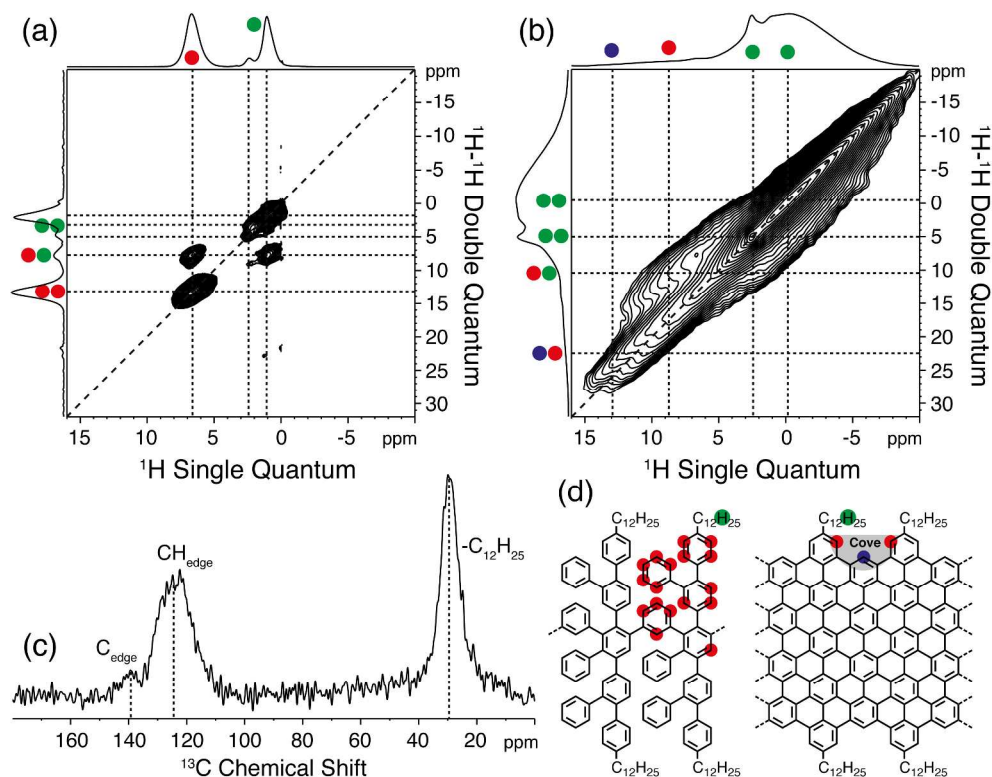


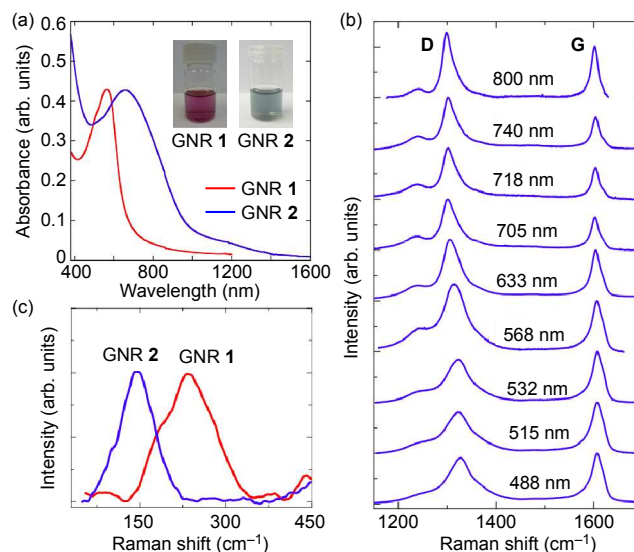
Figure 4 Solid-state NMR characterization of precursor **12** and GNR **2**. The 2D ^1H - ^1H DQ-SQ correlation spectra of (a) precursor **12** and (b) GNR **2** were recorded using a MAS frequency of 59524 Hz and two rotor periods of DQ recoupling. (c) 1D $^{13}\text{C}\{^1\text{H}\}$ REPT-HSQC spectrum recorded with a short REDOR recoupling period⁴⁰ of two rotor periods. (d) Assignment scheme.

UV-vis-NIR absorption and Raman spectroscopic analysis of GNR 2. Thanks to the long alkyl chains densely installed on the peripheral positions, GNR **2** could be dispersed in organic solvents such as tetrahydrofuran (THF), chlorobenzene, and *ortho*-dichlorobenzene (ODCB) under mild sonication. Some of the GNR powders remained undispersed even after extended sonication, which was similar to the observation during the debundling of CNTs⁴¹ as well as the exfoliation of graphene.⁴² This was presumably due to decreasing dispersibility of longer GNRs and/or stronger packing in some of the GNR aggregates, which could not be overcome by the

1
2
3 mild sonication. Nevertheless, larger aggregates could be removed by sedimentation or filtration
4 through a syringe filter (pore size: 5 μm), leaving pale blue dispersions with typical
5 concentrations of approximately 0.06 mg/mL without visible particles (Figure 5a, inset). The
6 relatively higher concentration of GNR **2** than the reported value for GNR **1**, i.e. ~ 0.01 mg/mL,¹⁶
7 is most probably due to inclusion of larger aggregates in dispersions of GNR **2**. GNR **2** showed
8 apparently lower dispersibility compared to that of GNR **1** due to stronger π - π interaction
9 between the extended aromatic cores. Nevertheless, it was still possible to spectroscopically
10 characterize GNR **2** in a dispersion as well as to process it from a liquid phase for microscopic
11 analyses (see below).
12
13
14
15
16
17
18
19
20
21
22
23

24 UV-vis-NIR absorption spectroscopic analysis of GNR **2** was thus performed on a
25 dispersion in THF (Figure 5a). GNRs **2-I** and **2-II** showed comparable spectra, indicating that
26 the longitudinal extension of both **2-I** and **2-II** was sufficient to reach the bandgap of the infinite
27 GNR (Figure S6a).¹⁶ Compared to the absorption spectrum of GNR **1**, that of GNR **2** displayed a
28 significantly broader absorption extending into the NIR region, with an absorption maximum at
29 660 nm. Whereas the absorption spectrum in 1,2,4-trichlorobenzene (TCB) was identical to the
30 one in THF, the spectrum measured in ODCB displayed a shifted absorption maximum at 645
31 nm (Figure S6b). This observation suggests a different degree of GNR aggregation in these
32 solvents, affecting the absorption profile.²⁶ The absorption edge was determined as the X-
33 intercept by extrapolation to be 1000 ± 20 nm, considering the variation in the absorption spectra
34 in TCB, THF, and ODCB. Although the effect of the aggregation cannot completely be
35 excluded, the optical bandgap of GNR **2** could be estimated from this absorption edge to be
36 1.24 ± 0.03 eV, which was in good agreement with the theoretical bandgap of 1.18 eV obtained
37 using density functional theory (DFT) calculations.⁵ This optical bandgap is considerably smaller
38
39
40
41
42
43
44
45
46
47
48
49
50
51
52
53
54
55
56
57
58
59
60

1
2
3 than the ~ 1.88 eV¹⁶ reported for GNR **1**, clearly demonstrating the lowering of the bandgap upon
4
5 increasing the lateral extension.
6
7
8
9



10
11
12
13
14
15
16
17
18
19
20
21
22
23
24
25
26
27
28
29 **Figure 5** (a) Normalized UV-vis-NIR absorption spectra of GNRs **1** and **2** in THF, inset:
30 photographs of dispersions of GNRs **1** and **2** in THF. (b) Raman spectra of GNR **2** measured
31 from 488 nm (2.54 eV) to 800 nm (1.55 eV) on a powder sample with laser power below 0.1
32 mW. (c) Acoustic region of the Raman spectra of GNRs **1** and **2**, measured at 515 nm (2.41 eV)
33 and 633 nm (1.96 eV), respectively, showing the RBLM peaks.
34
35
36
37
38
39
40
41
42
43

44 The Raman spectrum of GNR **2** displayed first-order D and G peaks (Figure 5b), which was
45 qualitatively similar to the Raman spectra of previously reported bottom-up synthesized GNRs.^{15,}
46
47
48
49
50
51
52
53
54
55
56
57
58
59
60
16, 18-20 GNR **2** with a width of ~ 2 nm demonstrated a distinct peak in the low-frequency region
(at ~ 170 cm⁻¹) that was assigned to the so-called radial breathing-like mode (RBLM) (Figure
5c).^{16, 20} The observation of this peak at a lower position, compared to that of the narrower GNR
1 with a width of ~ 1 nm (at ~ 235 cm⁻¹),¹⁶ further verified the uniform and laterally extended

1
2
3 structure of GNR **2**, since the RBLM peak is expected to shift to lower wavenumbers for
4 increasing width, in analogy to the radial breathing mode of carbon nanotubes.⁴³ Note however
5 that the exact RBLM peak position may also be affected by the specific edge geometry and
6 functional groups at the edges.
7
8
9
10
11

12 Profiting from the low bandgap for GNR **2**, for the first time, we were able to investigate
13 the Raman spectra of structurally defined GNRs over the visible and NIR energy ranges (Figure
14 5c), without any interference from the strong photoluminescence signals. This is in stark contrast
15 to GNR **1**, which could be measured only up to 633 nm.⁴⁴ The D peak of GNR **2** shifted to lower
16 wavenumber with increasing excitation wavelength. Notably, a small peak could clearly be
17 observed at the left side of the D peak with NIR excitation, whereas it appeared as a shoulder of
18 the D peak at smaller wavelengths. A shift of the RBLM was also observed, depending on the
19 excitation wavelength. Careful interpretations of these observations, involving extensive
20 theoretical studies, are expected to provide deeper insight into the phonon and electronic
21 dispersions of the GNRs, which will be reported elsewhere.
22
23
24
25
26
27
28
29
30
31
32
33
34
35

36 **Ultrafast THz photoconductivity analysis of GNR **2**.** The ultrafast photoconductivity of
37 GNR **2** dispersed in TCB was investigated through non-contact, time-resolved optical pump –
38 THz probe spectroscopy.⁴⁵ Whereas a study of the intrinsic electronic properties using device
39 measurements is challenging, THz spectroscopy provides a straightforward and non-invasive
40 approach to evaluate the photoconductivity within individual GNRs on ultrashort timescales.^{16, 46}
41 The lower bandgap of GNR **2** enabled photoconductivity studies over a wider range of pump
42 photon energies as compared to GNR **1**. Figure 6 shows the probe frequency resolved- (a) and
43 time dependent (b and c) complex conductivity of GNR **2** excited with a wavelength of 400 nm
44 (3.10 eV) and 800 nm (1.55 eV); both the frequency-dependent conductivity and the
45
46
47
48
49
50
51
52
53
54
55
56
57
58
59
60

1
2
3 conductivity dynamics are similar to those previously reported for GNR **1** at 400 nm
4 excitation.^{16, 46} Remarkably, the time-dependent photoconductivity of GNR **2** measured at 400
5
6 and 800 nm excitation are very similar. For both excitation energies, the dynamics show a quick
7
8 rise upon excitation followed by a fast decay in both the real and imaginary parts (Figure 6b and
9
10
11
12
13 c).

14
15 The lower optical absorption of GNR **2** due to the limited dispersibility made the
16
17 measurements more sensitive to losses of pump photons from scattering. The values for the
18
19 conductivity normalized to excitation density in Figure 6a should therefore be taken as
20
21 conservative estimates. Nevertheless, the observed magnitude of the real conductivity just after
22
23 excitation indicated a high photoconductivity of GNR **2**. Uncorrected for scattering of the pump
24
25 light, the inferred photoconductivity both at 400 nm and 800 nm excitation is comparable to that
26
27 of GNR **1**,^{16, 46} implying that the true photoconductivity of the broader GNR **2** is somewhat
28
29 larger than that of the narrower GNR **1**, as expected,³ given the smaller bandgap of GNR **2**.
30
31 Further, the frequency resolved photoconductivity of GNR **2** at 400 and 800 nm excitation
32
33 yielded a very similar shape, but with a slightly higher value for the scaled conductivity at 400
34
35 nm, suggesting a higher excitation quantum yield at 400 nm than at 800 nm.
36
37
38
39

40
41 Clearly, the THz spectroscopy measurements on GNR **2** demonstrate the generation of
42
43 conductive charge-carriers with excitation at both 800 nm and 400 nm, whereas GNR **1** showed a
44
45 response only at 400 nm. These results show that GNR **2** can be studied by pump-probe
46
47 spectroscopy techniques at a broader range of excitation wavelengths, allowing more detailed
48
49 investigations, for example, on the process of carrier multiplication⁴⁷⁻⁴⁹ in the GNRs.
50
51
52
53
54
55
56
57
58
59
60

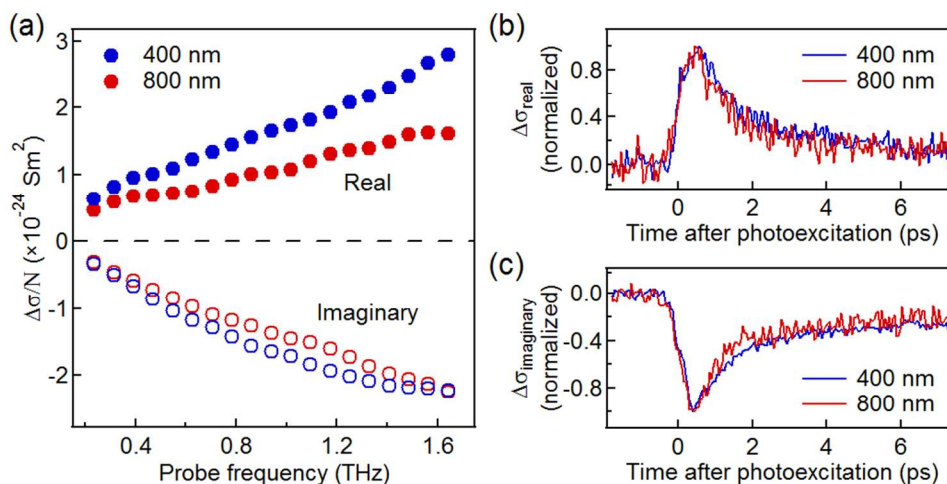
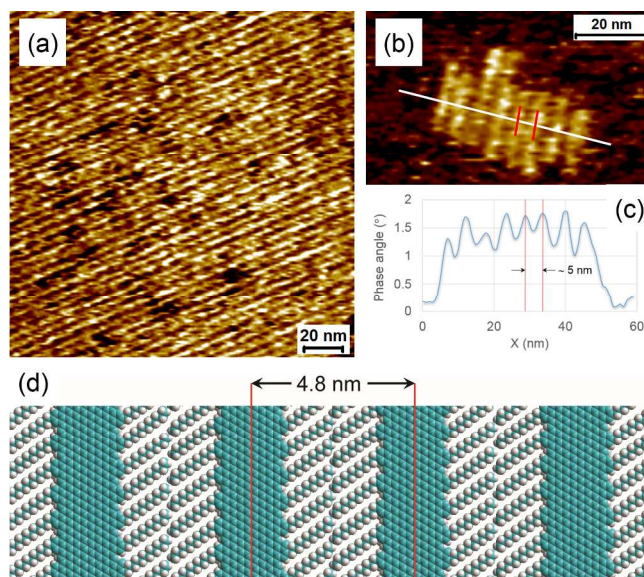


Figure 6 (a) Frequency-resolved, photoinduced complex conductivity of GNR **2** dispersed in TCB, scaled to the initial excitation density N , measured 0.5 ps after excitation by a 400 nm or 800 nm pulse. (b) Real and (c) imaginary components of the photoconductivity of GNR **2** as function of time after excitation. Absorbed pump fluence was 3.9×10^{18} photons/m² at 800 nm and 4.2×10^{18} photons/m² at 400 nm.

AFM visualization of GNR 2. Atomic force microscopy (AFM) analysis demonstrated the formation of well-ordered self-assembled monolayers on highly oriented pyrolytic graphite (HOPG), upon deposition of GNR **2-I** from a dispersion in hot TCB (120–130 °C) (Figures 7 and S7). The periodicity of the striped features was 5.0 ± 0.2 nm (Figure 7c), which was consistent with the ~ 4.8 nm expected lateral dimension of GNR **2** including the alkyl chains (Figure 7d). This observation indicated the adsorption of the GNRs next to each other without stacking or interdigitation of the alkyl chains. Whereas GNR **1** with the dodecyl chains showed partial stacking upon the formation of self-assembled monolayers,¹⁶ the absence of such stacking for GNR **2** could be explained by the enhanced interaction of the extended aromatic cores with the

1
2
3 HOPG surface. This result further attested the defined structure of GNR **2** with high uniformity,
4 and displayed its liquid-phase processability.
5
6

7
8 Highly covered areas extending several hundred nanometers in both lateral and longitudinal
9 directions were observed (Figure S8), suggesting end-to-end packing of the GNRs, given that the
10 average length of GNR **2-I** is ca. 30–56 nm. Indeed, the length of the GNRs in isolated small
11 domains was typically ca. 20–70 nm, which is in agreement with the estimated length (Figures
12 average length of GNR **2-I** is ca. 30–56 nm. Indeed, the length of the GNRs in isolated small
13 domains was typically ca. 20–70 nm, which is in agreement with the estimated length (Figures
14 7b and S9). Although monolayers of GNR **2-II** could not be visualized using AFM, presumably
15 due to its lower processability, this sample should contain long GNRs extending over 100 nm,
16 considering that GNR **2-II** was at least around three times longer than GNR **2-I**.
17
18
19
20
21
22
23
24
25
26



46 **Figure 7** (a), (b) AFM phase images of self-assembled monolayers of GNR **2-I** on HOPG (dry
47 film), showing (a) a large domain and (b) a small isolated domain. (c) Representative line profile,
48 which was measured along the white line in the phase image shown in panel b. (d) Molecular
49 model of GNR **2** displaying the packing of the GNRs in the self-assembled monolayer.
50
51
52
53
54
55
56
57
58
59
60

CONCLUSIONS

A bottom-up synthesis of laterally (~2 nm) as well as longitudinally (>100 nm) extended GNRs was achieved based on the *AB*-type Diels–Alder polymerization, displaying a low optical bandgap of approximately 1.24 eV. The efficient planarization (“graphitization”) of the polyphenylene precursor into the GNRs was corroborated by FTIR, NMR, UV–vis–NIR, and Raman spectroscopy. THz spectroscopy analysis revealed the high photoconductivity of the laterally extended GNRs. AFM analysis demonstrated the liquid-phase processability of such GNRs albeit with limited dispersibility. Remarkably, the broad absorption of the low-bandgap GNRs enabled their spectroscopic characterizations over the visible to NIR wavelengths, as represented by Raman and pump-probe THz spectroscopy studies. Further detailed spectroscopic investigations, including theoretical studies, are expected to elucidate some of the fundamental physical properties of such graphene nanostructures. Moreover, the synthetic method described potentially allows tuning of the width and bandgap for liquid-phase-processable GNRs by modifying the monomer architecture. This may not only enable the width-dependent studies on the single-GNR transistors but also contribute to the development of GNR-based optoelectronics, such as photodetectors and photovoltaics.

METHODS

Sample preparation. Full details regarding the synthesis and characterization of all the materials are provided in the Supporting Information.

Solid-state NMR. All solid-state MAS NMR experiments were recorded on a Bruker AVANCE-III 850 spectrometer operating at a Larmor frequency of 850.26 MHz (20.0 T). The

1
2
3 experiments employed a 1.3 mm H-X probe (Bruker) using a MAS frequency of 59524 Hz and a
4
5 recycle delay of 2 s. The 2D ^1H - ^1H DQ-SQ correlation spectra were acquired using the back-to-
6
7 back (BaBa) NMR dipolar recoupling sequence for both excitation and reconversion of DQ
8
9 coherences followed by a z-filter, set to one rotor period, prior to a final $\pi/2$ pulse for creating
10
11 transverse observable magnetization.³⁸ These experiments used two rotor periods (33.6 μs) of
12
13 BaBa recoupling blocks to excite/reconvert DQ coherences with 16 scans (full phase cycle) for
14
15 each of the 256 (precursor **12**) and 96 (GNR **2**) t_1 increments. A $\pi/2$ -pulse length of 1.5 μs
16
17 corresponding to an rf-field strength (ν_{rf}) of 167 kHz was used. The 1D $^{13}\text{C}\{^1\text{H}\}$ REPT-HSQC
18
19 spectrum of GNR **3** was recorded using two rotor periods of Rotational-Echo DOuble Resonance
20
21 (REDOR) recoupling for 10240 scans.⁴⁰ For the REDOR recoupling, $\pi/2$ -pulses of 1.8 μs were
22
23 used for both ^1H and ^{13}C , while low-power ^1H SW-f-TPPM decoupling was applied during
24
25 acquisition ($\nu_{\text{rf}} \sim 12$ kHz, 0.2 W).^{50, 51} Prior to all experiments the magic angle was checked using
26
27 KBr.⁵² ^1H and ^{13}C chemical shifts are reported relative to TMS using solid adamantane (^{13}C ,
28
29 38.484 ppm; ^1H , 1.85 ppm) as an external reference.^{53, 54}
30
31
32
33
34
35
36
37
38
39

40 **Raman spectroscopy.** Raman spectroscopy was performed in back-scattering geometry with
41
42 various spectrometers: a micro-Raman Witec single spectrometer was equipped with 532 nm
43
44 SSDP laser; multi-wavelength Raman spectra in the visible range were obtained with a Dilor
45
46 (Horiba-Jobin Yvon) triple spectrometer, equipped Ar-Kr laser, which possessed several laser
47
48 lines in the range from 488 nm to 568 nm, while for red and near-IR range we used a T64000
49
50 triple Raman spectrometer (Horiba-Jobin Yvon), equipped with He-Ne laser (633 nm) and the
51
52 tunable Ti:Sapphire laser (Coherent MBR-110) that covered the range from 705 nm to 915 nm.
53
54
55
56
57
58
59
60

1
2
3 The laser power was kept well below 0.1 mW to avoid heating or damaging the sample. The
4
5 laser spot was focused on the grain powder sample with a 100× long-distance objective.
6
7
8
9

10 **THz spectroscopy.** Sample solutions were placed in a quartz cuvette with an inner thickness
11
12 of 1 mm. Optical pump–THz probe measurements were performed using the output from a
13
14 titanium sapphire laser that generated pulses with a central wavelength of 800 nm, and a duration
15
16 of ~40 fs with a 1 kHz repetition rate. 400 nm excitation pulses were generated by frequency
17
18 doubling the 800 nm pulses in a Beta Barium Borate (BBO) crystal. Single-cycle probe pulses
19
20 comprising frequencies in the 0–2 THz range were generated from the 800 nm pulses in a 0.5
21
22 mm thick <110> ZnTe crystal by a process called optical rectification.⁴⁵ Beyond the sample, the
23
24 transmitted THz field was detected with a third 800 nm pulse in a second <110> ZnTe crystal
25
26 using the electro-optic effect.⁴⁵ By mechanically delaying the detection pulse, the whole
27
28 waveform of the THz pulse could be measured, and the frequency-resolved conductivity could
29
30
31
32
33
34 be obtained as described in Refs. 16 and 46.
35
36
37
38

39 **AFM analysis.** A Multimode AFM with a Nanoscope IV controller (Veeco/Digital
40
41 Instruments) was employed in intermittent contact mode. Prior to AFM measurements, GNR
42
43 powder was dispersed in TCB by ultrasonication for 2 h followed by heating at 120–130 °C for
44
45 15 minutes. A drop of this hot dispersion was applied to a hot HOPG surface, which was also
46
47 held at 120 °C. After the hot deposition, the HOPG sample was heated for another 15 minutes.
48
49 The surface was then washed with 2 mL of TCB and heated again to ensure complete
50
51 evaporation of the solvent. THF could alternatively be used as a solvent for washing. AFM
52
53 images were recorded at room temperature and processed using SPIP (Image Metrology)
54
55
56
57
58
59
60

1
2
3 software. The width of the GNRs was obtained from analysis of AFM images using two different
4
5 methods, namely, manual and automated power spectrum density (PSD) analysis. In the first
6
7 method, the width of the GNRs was measured manually by drawing line profiles across the GNR
8
9 domains in an AFM image and averaging over many of such domains. In the second method, an
10
11 automated power spectral density analysis was performed on AFM images, which essentially
12
13 furnished peaks corresponding to the periodic features present in the AFM images (Figure S10).
14
15 While the periodicity obtained from manual analysis was 5.0 ± 0.2 nm, the automated analysis
16
17 furnished a periodicity of 5.2 ± 0.2 nm.
18
19
20
21
22
23

24
25 *Conflict of Interest:* Authors declare no competing financial interest.
26
27

28
29 *Acknowledgement.* We are grateful to the financial support from European Research Council
30
31 grant on NANOGRAPH, DFG Priority Program SPP 1459, Graphene Flagship (No. CNECT-
32
33 ICT-604391), and European Union Projects UPGRADE, GENIUS, and MoQuaS. C.C. and
34
35 I.A.V. acknowledge the Humboldt Foundation in the framework of the Sofja Kovalevskaja
36
37 award. M.R.H. acknowledges the Villum Foundation under the Young Investigator Programme
38
39 (VKR023122).
40
41
42

43
44 *Supporting Information Available:* Experimental details; additional discussion on the
45
46 fractionation of polyphenylene precursor **12**; SEC profiles; full FTIR spectra; additional UV–
47
48 vis–NIR absorption spectra; additional AFM images; and NMR spectra. This material is
49
50 available free of charge *via* the Internet at <http://pubs.acs.org>.
51
52
53
54
55
56
57
58
59
60

REFERENCES AND NOTES

1. Li, X.; Wang, X.; Zhang, L.; Lee, S.; Dai, H. Chemically Derived, Ultrasoft Graphene Nanoribbon Semiconductors. *Science* **2008**, 319, 1229-1232.
2. Bai, J.; Huang, Y. Fabrication and Electrical Properties of Graphene Nanoribbons. *Mater. Sci. Eng. R-Rep.* **2010**, 70, 341-353.
3. Obradovic, B.; Kotlyar, R.; Heinz, F.; Matagne, P.; Rakshit, T.; Giles, M. D.; Stettler, M. A.; Nikonov, D. E. Analysis of Graphene Nanoribbons as a Channel Material for Field-Effect Transistors. *Appl. Phys. Lett.* **2006**, 88, 142102.
4. Wang, J.; Zhao, R.; Yang, M.; Liu, Z. Inverse Relationship between Carrier Mobility and Bandgap in Graphene. *J. Chem. Phys.* **2013**, 138, 084701.
5. Osella, S.; Narita, A.; Schwab, M. G.; Hernandez, Y.; Feng, X.; Müllen, K.; Beljonne, D. Graphene Nanoribbons as Low-Band-Gap Donor Materials for Organic Photovoltaics: Quantum-Chemical Aided Design. *ACS Nano* **2012**, 6, 5539-5548.
6. Ritter, K. A.; Lyding, J. W. The Influence of Edge Structure on the Electronic Properties of Graphene Quantum Dots and Nanoribbons. *Nature Mater.* **2009**, 8, 235-242.
7. Chen, Z.; Lin, Y.; Rooks, M.; Avouris, P. Graphene Nano-Ribbon Electronics. *Physica E* **2007**, 40, 228-232.
8. Han, M.; Özyilmaz, B.; Zhang, Y.; Kim, P. Energy Band-Gap Engineering of Graphene Nanoribbons. *Phys. Rev. Lett.* **2007**, 98, 206805.
9. Abbas, A. N.; Liu, G.; Liu, B.; Zhang, L.; Liu, H.; Ohlberg, D.; Wu, W.; Zhou, C. Patterning, Characterization, and Chemical Sensing Applications of Graphene Nanoribbon Arrays Down to 5 nm Using Helium Ion Beam Lithography. *ACS Nano* **2014**, 8, 1538-1546.
10. Kosynkin, D. V.; Higginbotham, A. L.; Sinitskii, A.; Lomeda, J. R.; Dimiev, A.; Price, B. K.; Tour, J. M. Longitudinal Unzipping of Carbon Nanotubes to Form Graphene Nanoribbons. *Nature* **2009**, 458, 872-876.
11. Jiao, L.; Zhang, L.; Wang, X.; Diankov, G.; Dai, H. Narrow Graphene Nanoribbons from Carbon Nanotubes. *Nature* **2009**, 458, 877-880.
12. Jiao, L. Y.; Wang, X. R.; Diankov, G.; Wang, H. L.; Dai, H. J. Facile Synthesis of High-Quality Graphene Nanoribbons. *Nature Nanotech.* **2010**, 5, 321-325.
13. Yang, X. Y.; Dou, X.; Rouhanipour, A.; Zhi, L. J.; Rader, H. J.; Müllen, K. Two-Dimensional Graphene Nanoribbons. *J. Am. Chem. Soc.* **2008**, 130, 4216-4217.
14. Dössel, L.; Gherghel, L.; Feng, X.; Müllen, K. Graphene Nanoribbons by Chemists: Nanometer-Sized, Soluble, and Defect-Free. *Angew. Chem. Int. Ed.* **2011**, 50, 2540-2543.
15. Schwab, M. G.; Narita, A.; Hernandez, Y.; Balandina, T.; Mali, K. S.; De Feyter, S.; Feng, X.; Müllen, K. Structurally Defined Graphene Nanoribbons with High Lateral Extension. *J. Am. Chem. Soc.* **2012**, 134, 18169-18172.
16. Narita, A.; Feng, X.; Hernandez, Y.; Jensen, S. A.; Bonn, M.; Yang, H.; Verzhbitskiy, I. A.; Casiraghi, C.; Hansen, M. R.; Koch, A. H. R., *et al.* Structurally Well-Defined and Liquid-Phase-Processable Graphene Nanoribbons. *Nature Chem.* **2014**, 6, 126-132.
17. Tan, Y.-Z.; Tang, B.; Parvez, K.; Narita, A.; Osella, S.; Beljonne, D.; Feng, X.; Müllen, K. Atomically Precise Edge Chlorination of Nanographenes and Its Application to Graphene Nanoribbons. *Nat. Commun.* **2013**, 4, 2646.
18. Vo, T. H.; Shekhiriev, M.; Kunkel, D. A.; Morton, M. D.; Berglund, E.; Kong, L.; Wilson, P. M.; Dowben, P. A.; Enders, A.; Sinitskii, A. Large-Scale Solution Synthesis of Narrow Graphene Nanoribbons. *Nat. Commun.* **2014**, 5, 3189.

19. Vo, T. H.; Shekhirev, M.; Kunkel, D. A.; Orange, F.; Guinel, M. J. F.; Enders, A.; Sinitskii, A. Bottom-up Solution Synthesis of Narrow Nitrogen-Doped Graphene Nanoribbons. *Chem. Commun.* **2014**, 50, 4172–4174.
20. Cai, J.; Ruffieux, P.; Jaafar, R.; Bieri, M.; Braun, T.; Blankenburg, S.; Muoth, M.; Seitsonen, A. P.; Saleh, M.; Feng, X., *et al.* Atomically Precise Bottom-up Fabrication of Graphene Nanoribbons. *Nature* **2010**, 466, 470-473.
21. Bronner, C.; Stremlau, S.; Gille, M.; Brauße, F.; Haase, A.; Hecht, S.; Tegeder, P. Aligning the Band Gap of Graphene Nanoribbons by Monomer Doping. *Angew. Chem. Int. Ed.* **2013**, 52, 4422-4425.
22. Chen, Y.-C.; de Oteyza, D. G.; Pedramrazi, Z.; Chen, C.; Fischer, F. R.; Crommie, M. F. Tuning the Band Gap of Graphene Nanoribbons Synthesized from Molecular Precursors. *ACS Nano* **2013**, 7, 6123-6128.
23. Zhang, Y.; Zhang, Y.; Li, G.; Lu, J.; Lin, X.; Du, S.; Berger, R.; Feng, X.; Müllen, K.; Gao, H.-J. Direct Visualization of Atomically Precise Nitrogen-Doped Graphene Nanoribbons. *Appl. Phys. Lett.* **2014**, 105, 023101.
24. Yang, F.; Wang, X.; Zhang, D.; Yang, J.; LuoDa; Xu, Z.; Wei, J.; Wang, J.-Q.; Xu, Z.; Peng, F., *et al.* Chirality-Specific Growth of Single-Walled Carbon Nanotubes on Solid Alloy Catalysts. *Nature* **2014**, 510, 522-524.
25. Omachi, H.; Nakayama, T.; Takahashi, E.; Segawa, Y.; Itami, K. Initiation of Carbon Nanotube Growth by Well-Defined Carbon Nanorings. *Nature Chem.* **2013**, 5, 572-576.
26. Abbas, A. N.; Liu, G.; Narita, A.; Orosco, M.; Feng, X.; Müllen, K.; Zhou, C. Deposition, Characterization, and Thin-Film-Based Chemical Sensing of Ultra-Long Chemically Synthesized Graphene Nanoribbons. *J. Am. Chem. Soc.* **2014**, 136, 7555-7558.
27. Qian, G.; Wang, Z. Y. Near-Infrared Organic Compounds and Emerging Applications. *Chem. Asian J.* **2010**, 5, 1006-1029.
28. Jorio, A.; Saito, R.; Dresselhaus, G.; Dresselhaus, M. S. *Raman Spectroscopy in Graphene Related Systems*. Wiley-VCH Verlag: Weinheim, **2011**.
29. Liu, P.; Chen, Y.; Deng, J.; Tu, Y. An Efficient Method for the Preparation of Benzylic Bromides. *Synthesis* **2001**, 14, 2078-2080.
30. Shifrina, Z. B.; Averina, M. S.; Rusanov, A. L.; Wagner, M.; Müllen, K. Branched Polyphenylenes by Repetitive Diels-Alder Cycloaddition. *Macromolecules* **2000**, 33, 3525-3529.
31. Kumar, U.; Neenan, T. X. Diels-Alder Polymerization between Bis(cyclopentadienones) and Acetylenes. A Versatile Route to New Highly Aromatic Polymers. *Macromolecules* **1995**, 28, 124-130.
32. Centrone, A.; Brambilla, L.; Renouard, T.; Gherghel, L.; Mathis, C.; Müllen, K.; Zerbi, G. Structure of New Carbonaceous Materials: The Role of Vibrational Spectroscopy. *Carbon* **2005**, 43, 1593-1609.
33. Schmidt-Rohr, K.; Spiess, H. W. *Multidimensional Solid-State NMR and Polymers*. Academic Press: New York, **1994**.
34. Shu, J.; Dudenko, D.; Esmaeili, M.; Park, J. H.; Puniredd, S. R.; Chang, J. Y.; Breiby, D. W.; Pisula, W.; Hansen, M. R. Coexistence of Helical Morphologies in Columnar Stacks of Star-Shaped Discotic Hydrazones. *J. Am. Chem. Soc.* **2013**, 135, 11075-11086.
35. Brown, S. P.; Schnell, I.; Brand, J. D.; Müllen, K.; Spiess, H. W. An Investigation of π - π Packing in a Columnar Hexabenzocoronene by Fast Magic-Angle Spinning and Double-Quantum 1H Solid-State NMR Spectroscopy. *J. Am. Chem. Soc.* **1999**, 121, 6712-6718.

- 1
2
3 36. Ochsensfeld, C.; Brown, S. P.; Schnell, I.; Gauss, J.; Spiess, H. W. Structure Assignment
4 in the Solid State by the Coupling of Quantum Chemical Calculations with NMR Experiments:
5 A Columnar Hexabenzocoronene Derivative. *J. Am. Chem. Soc.* **2001**, 123, 2597-2606.
- 6 37. Hansen, M. R.; Feng, X.; Macho, V.; Müllen, K.; Spiess, H. W.; Floudas, G. Fast and
7 Slow Dynamics in a Discotic Liquid Crystal with Regions of Columnar Order and Disorder.
8 *Phys. Rev. Lett.* **2011**, 107, 257801.
- 9 38. Feike, M.; Demco, D. E.; Graf, R.; Gottwald, J.; Hafner, S.; Spiess, H. W. Broadband
10 Multiple-Quantum NMR Spectroscopy. *J. Magn. Reson. Ser. A* **1996**, 122, 214-221.
- 11 39. Saalwächter, K.; Lange, F.; Matyjaszewski, K.; Huang, C.-F.; Graf, R. BaBa-xy16:
12 Robust and Broadband Homonuclear DQ Recoupling for Applications in Rigid and Soft Solids
13 up to the Highest MAS Frequencies. *J. Magn. Reson.* **2011**, 212, 204-215.
- 14 40. Saalwächter, K.; Schnell, I. REDOR-Based Heteronuclear Dipolar Correlation
15 Experiments in Multi-Spin Systems: Rotor-Encoding, Directing, and Multiple Distance and
16 Angle Determination. *Solid State Nucl. Magn. Reson.* **2002**, 22, 154-187.
- 17 41. Giordani, S.; Bergin, S. D.; Nicolosi, V.; Lebedkin, S.; Kappes, M. M.; Blau, W. J.;
18 Coleman, J. N. Debundling of Single-Walled Nanotubes by Dilution: Observation of Large
19 Populations of Individual Nanotubes in Amide Solvent Dispersions. *J. Phys. Chem. B* **2006**, 110,
20 15708-15718.
- 21 42. Hernandez, Y.; Nicolosi, V.; Lotya, M.; Blighe, F. M.; Sun, Z.; De, S.; McGovern, I. T.;
22 Holland, B.; Byrne, M.; Gun'Ko, Y. K., *et al.* High-Yield Production of Graphene by Liquid-
23 Phase Exfoliation of Graphite. *Nature Nanotech.* **2008**, 3, 563-568.
- 24 43. Saito, R.; Hofmann, M.; Dresselhaus, G.; Jorio, A.; Dresselhaus, M. S. Raman
25 Spectroscopy of Graphene and Carbon Nanotubes. *Adv. Phys.* **2011**, 60, 413-550.
- 26 44. Detailed Raman studies on GNR **1** will be published elsewhere.
- 27 45. Ulbricht, R.; Hendry, E.; Shan, J.; Heinz, T.; Bonn, M. Carrier Dynamics in
28 Semiconductors Studied with Time-Resolved Terahertz Spectroscopy. *Rev. Mod. Phys.* **2011**, 83,
29 543-586.
- 30 46. Jensen, S. A.; Ulbricht, R.; Narita, A.; Feng, X.; Müllen, K.; Hertel, T.; Turchinovich, D.;
31 Bonn, M. Ultrafast Photoconductivity of Graphene Nanoribbons and Carbon Nanotubes. *Nano*
32 *Lett.* **2013**, 13, 5925-5930.
- 33 47. Tielrooij, K. J.; Song, J. C. W.; Jensen, S. A.; Centeno, A.; Pesquera, A.; Zurutuza
34 Elorza, A.; Bonn, M.; Levitov, L. S.; Koppens, F. H. L. Photoexcitation Cascade and Multiple
35 Hot-Carrier Generation in Graphene. *Nature Phys.* **2013**, 9, 248-252.
- 36 48. Ueda, A.; Matsuda, K.; Tayagaki, T.; Kanemitsu, Y. Carrier Multiplication in Carbon
37 Nanotubes Studied by Femtosecond Pump-Probe Spectroscopy. *Appl. Phys. Lett.* **2008**, 92,
38 233105.
- 39 49. Pijpers, J. J. H.; Ulbricht, R.; Tielrooij, K. J.; Osherov, A.; Golan, Y.; Delerue, C.; Allan,
40 G.; Bonn, M. Assessment of Carrier-Multiplication Efficiency in Bulk PbSe and PbS. *Nature*
41 *Phys.* **2009**, 5, 811-814.
- 42 50. Thakur, R. S.; Kurur, N. D.; Madhu, P. K. Swept-Frequency Two-Pulse Phase
43 Modulation for Heteronuclear Dipolar Decoupling in Solid-State NMR. *Chem. Phys. Lett.* **2006**,
44 426, 459-463.
- 45 51. Paul, S.; Kurur, N. D.; Madhu, P. K. On the Choice of Heteronuclear Dipolar Decoupling
46 Scheme in Solid-State NMR. *J. Magn. Reson.* **2010**, 207, 140-148.
- 47 52. Frye, J. S.; Maciel, G. E. Setting the Magic Angle Using a Quadrupolar Nuclide. *J.*
48 *Magn. Reson.* **1982**, 48, 125-131.
- 49
50
51
52
53
54
55
56
57
58
59
60

- 1
2
3 53. Hayashi, S.; Hayamizu, K. Chemical Shift Standards in High-Resolution Solid-State
4 NMR (^{13}C , ^{29}Si , and ^1H Nuclei. *Bull. Chem. Soc. Jpn.* **1991**, 64, 685-687.
5
6 54. Morcombe, C. R.; Zilm, K. W. Chemical Shift Referencing in MAS Solid State NMR. *J.*
7 *Magn. Reson.* **2003**, 162, 479-486.
8
9
10

11 TOC GRAPHIC

